A&A, 710, A196 (2026)
https://doi.org/10.1051/0004-6361/202557431
© The Authors 2026

Astronomy & Astrophysics

Accurate distances of the Galactic spiral arms from dust-scattered X-ray emission of gamma-ray bursts

B. Vaia[1,2,3,⋆], I. Fornasiero[1,2,3], A. Tiengo[1,3], A. Bracco[4,5], V. Jelić[6], Ž. Bošnjak[7], F. Pintore[8], and P. Esposito[1,3]

[1] Scuola Universitaria Superiore IUSS Pavia, Piazza della Vittoria 15, 27100 Pavia, Italy
[2] Department of Physics, University of Trento, Via Sommarive 14, 38123 Povo (TN), Italy
[3] Istituto Nazionale di Astrofisica, Istituto di Astrofisica Spaziale e Fisica Cosmica di Milano, via A. Corti 12, 20133 Milano, Italy
[4] INAF – Osservatorio Astrofisico di Arcetri, Largo E. Fermi 5, 50125 Firenze, Italy
[5] Laboratoire de Physique de l'Ecole Normale Supérieure, ENS, Université PSL, CNRS, Sorbonne Université, Université de Paris, F-75005 Paris, France
[6] Ruđer Bošković Institute, Bijeńicka cesta 54, 10000 Zagreb, Croatia
[7] University of Zagreb Faculty of Electrical Engineering and Computing, Unska ul. 3, 10000 Zagreb, Croatia
[8] INAF – Istituto di Astrofisica Spaziale e Fisica Cosmica di Palermo, Via U. La Malfa 153, 90146 Palermo, Italy

Received 26 September 2025 / Accepted 27 April 2026

ABSTRACT

The details of the spiral structure of the Milky Way are still debated due to the large uncertainties in the distance estimates obtained through the most common tracers. However, X-ray dust scattering rings produced by short extragalactic X-ray transients provide a direct method to measure the 3D distribution of interstellar clouds up to the edges of our Galaxy with a precision of a few percent. We report on an analysis of all the available *XMM-Newton* and *Chandra* follow-up observations of three low-latitude gamma-ray bursts: GRB 031203 ($l \simeq 255°$, $b \simeq -5°$), GRB 160623A ($l \simeq 84°$, $b \simeq -3°$), and GRB 221009A ($l \simeq 53°$, $b \simeq 4°$). The previous detection of X-ray rings in these observations, produced by dust clouds located beyond 5 kpc, can be associated with dust in the Perseus, Outer, and Outer Scutum-Centaurus arms, thus providing direct distance measurements to these structures along three distinct lines of sight. We identify two additional rings in the direction of GRB 160623A produced by dusty clouds at 6.91 ± 0.06 kpc and 9.9 ± 0.6 kpc, and we confirm – through a second *XMM-Newton* observation – the presence of one cloud at 9.7 ± 0.4 kpc toward GRB 031203. We also accurately measured the distance of dusty clouds up to 19.0 ± 0.2 kpc based on the analysis of one *Chandra* and four *XMM-Newton* observations of GRB 221009A. The small statistical and systematic uncertainties of these measurements place tight constraints on the geometry of the outer Milky Way and reveal significant deviations from current models, which critically depend on spectroscopy-based Galactic rotation curves at large distances.

Key words. dust, extinction – Galaxy: structure – X-rays: ISM – gamma-ray burst: individual: GRB 031203 – gamma-ray burst: individual: GRB 160623A – gamma-ray burst: individual: GRB 221009A

1. Introduction

Despite extensive studies throughout the past century, the exact spiral structure of the Milky Way is still not well defined. The Galactic structure is reconstructed on the basis of different tracers whose distance is often affected by large uncertainties arising from kinematic distance ambiguities and dependence on a Galactic rotation curve model.

The most widely used tracers (e.g., Kalberla et al. 2005; Green et al. 2009; Hou & Han 2014; Reid et al. 2019) are 6.7 GHz methanol masers, giant molecular clouds, H II regions, and clouds of neutral atomic hydrogen (H I). H II regions and methanol masers are predominantly associated with star-forming regions, and giant molecular clouds serve as the birthplaces of massive stars. Because of this, their spatial distribution is expected to be consistent with that of the Galactic young stellar population.

Unlike visible light from stars, the radio recombination lines emitted by H II regions and the spectral lines from methanol masers are largely unaffected by absorption in the interstellar medium (ISM). This makes them particularly useful for probing distant and obscured regions of the Milky Way (e.g., Anderson et al. 2011; Breen et al. 2015). When it comes to identifying molecular clouds, the most commonly used tracer is carbon monoxide (CO). Carbon monoxide is the second most abundant molecule in the ISM after molecular hydrogen (H_2). Directly observing H_2, however, is highly challenging due to the lack of a permanent dipole moment. For these reasons, our knowledge of the spiral structure of the Milky Way is primarily based on CO surveys such as the CfA-Chile (Dame et al. 2001; Dame & Thaddeus 2022), the FCRAO Galactic Ring Survey and Outer Galaxy Survey (Heyer et al. 2001; Roman-Duval et al. 2010), and SEDIGISM (Schuller et al. 2021). Another key component for tracing the Galactic structure is H I, the most abundant element in the ISM, observed through the 21 cm hyperfine transition line. Surveys such as HIPASS (Barnes et al. 2001), GALFA-HI (Peek et al. 2011), GASS (McClure-Griffiths et al. 2009; Kalberla et al. 2010; Kalberla & Haud 2015), and EBHIS (Winkel et al. 2016) have played a crucial role in mapping the distribution of the ISM. In parallel with tracer-based catalogs, the Galactic spiral structure has also been investigated through top-down reconstructions based on radial velocity measurements. In this approach, spectroscopic observations of extended H I or CO

⋆ Corresponding author: beatrice.vaia@inaf.it

Open Access article, published by EDP Sciences, under the terms of the Creative Commons Attribution License (https://creativecommons.org/licenses/by/4.0), which permits unrestricted use, distribution, and reproduction in any medium, provided the original work is properly cited.
This article is published in open access under the Subscribe to Open model. Subscribe to A&A to support open access publication.

emission are combined with an assumed Galactic rotation curve to convert line-of-sight velocities into galactocentric positions, producing maps of the Milky Way disk. Classical examples are the H I-based reconstructions of Levine et al. (2006) and the work of Miville-Deschênes et al. (2017), derived from a hierarchical decomposition of CO emission over the entire Galactic plane. The choice and accuracy of the rotation curve are therefore crucial to assigning kinematic distances of Galactic objects. Many rotation curve models have been developed over the past decades (such as the ones of Clemens 1985; Persic et al. 1996; Eilers et al. 2019; Reid et al. 2019), but significant uncertainties still persist, mainly regarding the distribution of the dark matter component in the outer regions.

In 2013, the launch of the ESA Gaia satellite (Gaia Collaboration 2016) revolutionized the study of the structure of the Milky Way by providing precise astrometric measurements of stars (e.g., Sale & Magorrian 2018; Chen et al. 2018; Green et al. 2019; Hottier et al. 2020; Rezaei Kh. et al. 2020; Lallement et al. 2022). However, stellar distances measured by Gaia are available only up to a few kiloparsecs. To explore more distant regions of the Galactic plane, extinction maps based on infrared data can be utilized. Over the years, significant work has been done in this field. For instance, Schlegel et al. (1998) used far-infrared dust emission data from the IRAS and COBE satellites to create an all-sky dust column density map. In 2006, Lombardi et al. (2006) employed 2MASS photometric data and the color excess technique to study molecular clouds, while Schlafly et al. (2010) used data from the Sloan Digital Sky Survey (SDSS). Rezaei et al. (2024) produced a 3D map of the Milky Way's plane extending up to 10 kpc using near-infrared data from the SDSS Apache Point Observatory Galactic Evolution Experiment (APOGEE). Another 3D dust map obtained by combining Gaia parallaxes with large photometric surveys has been published recently by Zucker et al. (2025). However, this map is limited to a confined portion of the Galactic plane only observable from the southern hemisphere, and depending on the sight lines, it probes distances up to only ~5–10 kpc.

Recent studies of the Milky Way's structure (Hou & Han 2014) suggest that our Galaxy has four spiral arms, which contrasts with earlier models that indicated only two arms (Oort et al. 1958). However, uncertainties persist regarding the exact morphology of the Milky Way. For example, only in 2011 Dame & Thaddeus (2011) identified a new spiral arm beyond the Outer Arm at ≃15 kpc from the Galactic center, at longitudes from 13° to 55° in the first quadrant. This new arm was discovered by studying CO emission. It was overlooked in existing 21 cm surveys probably because it is highly inclined relative to the Galactic plane.

X-ray dust scattering rings observed around gamma-ray bursts (GRBs) provide a unique opportunity to measure the distances to Galactic interstellar clouds (Šiljeg et al. 2023). These rings are formed by the prompt X-ray emission of the gamma-ray burst, whose photons reach the observer with an increasingly larger delay and angular offset due to scattering within the intervening dust clouds. The accuracy of this method is very good up to large distances, allowing the distances of the outermost spiral arms to be tightly constrained. For an extragalactic X-ray source and a dust cloud within our Galaxy, the angular size of the observed dust-scattering ring is given by

$$\theta[\mathrm{arcmin}] = 4.455 \sqrt{\frac{\Delta t[\mathrm{days}]}{D_\mathrm{d}[\mathrm{kpc}]}}, \quad (1)$$

where Δt represents the time delay between the direct and scattered X-rays and D_d is the distance to the dust cloud.

To constrain the structure of our Galaxy, particularly focusing on the most distant arms, we identified three low-latitude ($|b| < 5°$) GRBs around which X-ray scattering rings have been detected by *XMM-Newton* or *Chandra*: GRB 221009A ($l \simeq 53°$, $b \simeq 4°$; Tiengo et al. 2023; Williams et al. 2023), GRB 160623A ($l \simeq 84°$, $b \simeq -3°$; Pintore et al. 2017), and GRB 031203 ($l \simeq 255°$, $b \simeq -5°$; Vaughan et al. 2004; Tiengo & Mereghetti 2006; Feng & Fox 2010). These measurements can be used to constrain the structure of the Perseus, Outer, and Outer Scutum-Centaurus (OSC) arms. This paper is structured as follows: In Sect. 2 we describe the data reduction process, in Sect. 3 we explain the analysis methodology and report the results, which are discussed in Sect. 4. Finally, Sect. 5 presents the conclusions.

2. Observations and data reduction

In this work we report on an analysis of X-ray data collected by the *XMM-Newton* (Jansen et al. 2001) and *Chandra* (Weisskopf et al. 2000) missions (Obs IDs in Table 1). The study of X-ray expanding rings requires a detailed characterization of the spatial distribution of the background signal (i.e., the instrumental and diffuse X-ray contribution unrelated to the source), which we obtained either through the use of archival observations or counts from the same observation but in a different energy band.

For the *XMM-Newton* observations, we analyzed data from the EPIC pn camera (Strüder et al. 2001) and the two EPIC Metal-Oxide Semiconductor (MOS; Turner et al. 2001) cameras. These data were processed using the Science Analysis Software (SAS) 20.0.0 (Gabriel et al. 2004) and the latest calibration files. The EPIC events were cleaned with standard filtering expressions[1]. Point-like sources, identified through the SAS source detection task `emldetect`, were excluded by masking circular regions, each with a radius of 25″ (except for particularly bright sources, where the radius was set to 40″).

For most *XMM-Newton* observations, the pn background was extracted over a broad energy range of 0.5–15 keV. We excluded two intervals: the band containing significant ring emission (0.7–4 keV for GRB 221009A and GRB 160623A, and 0.8–2.2 keV for GRB 031203) and the 7.3–9.3 keV region. The latter contains fluorescence features from the detectors and their surrounding structure, whose intensity is not uniform across the pn camera[2]. For the MOS cameras, we adopted a similar strategy, extracting the background from the 4–12 keV range.

The background events extracted in this way were treated as an independent sample and analyzed following the same procedure adopted for the source regions. In particular, a pseudo-distance was assigned to the background events producing a background pseudo-distance distribution. Before subtraction, this distribution extracted from an energy range where no dust-scattering emission was observed had to be rescaled by the ratio of the number of counts detected in the source and background energy ranges in a spatial region where no dust-scattering signal is expected at any energy.

The *Chandra* data reduction was performed with the Chandra Interactive Analysis of Observations (`CIAO v4.15`; Fruscione et al. 2006) software and the calibration data files

[1] For pn data: `#XMMEA_EP&&(FLAG==0)&&(PATTERN<=4)` and for MOS: `#XMMEA_EM&&(PATTERN<=12)`.

[2] This band contains the emission lines corresponding to Cu-Kα, Ni-Kα, and Zn-Kα.

CALDB(v4.10.2). In order to reprocess the data, the chandra_repro script was used, while the blank-sky script automatically selected the appropriate blank-sky background files in each observation. Point-like sources were identified using the wavdetect tool and excluded from the analysis.

2.1. GRB 221009A

GRB 221009A was initially reported by the Burst Alert Telescope (BAT) aboard the *Swift Neil Gehrels* Observatory on October 9, 2022, at 14:10:17 UT (Dichiara et al. 2022). However, the GRB started about an hour before, as observed for example by the *Fermi* Gamma-ray Burst Monitor (GBM; Lesage et al. 2023). This GRB is the brightest ever recorded and occurred near the direction of the Galactic plane, producing multiple X-ray dust scattering rings that were later observed by the X-ray Telescope (XRT) on *Swift* (Williams et al. 2023; Vasilopoulos et al. 2023; Vaia et al. 2025) as well as by *XMM-Newton* (Tiengo et al. 2023; Vaia et al. 2025), the Imaging X-ray Polarimetry Explorer (IXPE: Negro et al. 2023), and *Chandra*. For this study, we focus on data from *XMM-Newton* and *Chandra*, which are more sensitive to the relatively small and faint rings produced by distant dust.

2.1.1. XMM-Newton observations

XMM-Newton observed GRB 221009A on five occasions from October 11 to November 11, 2022. To minimize pile-up during the first observation, the pn and the two MOS cameras were operated in Timing mode, using the thick optical-blocking filter. In Timing mode, only the peripheral CCDs of the MOS cameras provide full imaging capabilities, covering a region from approximately 5′ to 15′ from the target position. As a result, only the rings produced by clouds at distances smaller than 1.6 kpc (see Eq. 1) are visible in this observation (Tiengo et al. 2023; Vaia et al. 2025). This dataset was not used in this work, as we focused on clouds at distances greater than 5 kpc. The log of all the observations analysed in this work is reported in Table 1.

As a background for Obs2, we selected, for both cameras, data from the observation of the bright high-redshift quasar RBS 315 conducted in January 2013 (Observation ID: 0690900201). As in Vaia et al. (2025), this observation was chosen due to the similarities of the central source with the GRB 221009A X-ray afterglow and because it occurred during a similar phase of the solar cycle, ensuring comparable contamination from the unfocused particle background (Gastaldello et al. 2022). We adopted this strategy for the background to subtract the contribution from the X-ray background as well as from the GRB afterglow and its possible dust-scattering halo. The approach outlined at the beginning of Sect. 2 was instead applied to the remaining three *XMM-Newton* observations. To maximize the signal-to-noise ratio of the rings, the analysis was confined to the 0.7–4 keV energy band, as in Tiengo et al. (2023) and Vaia et al. (2025).

2.1.2. Chandra observation

The *Chandra* telescope started observing GRB 221009A on October 17, 2022, at 16:53:32 UT with an exposure time of 21.7 ks (Table 1). The data were acquired using the ACIS-I instrument in FAINT mode. As shown in Fig. 1, the rings are not fully covered and only a portion of them is visible since the observation was performed off-axis. This strategy was chosen to exclude the afterglow emission and allow for the detection of the largest rings.

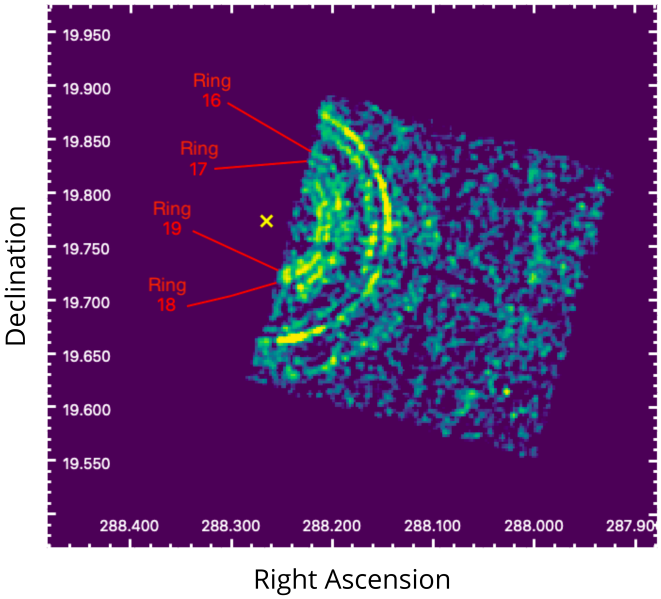


Fig. 1. ACIS-I *Chandra* image of GRB 221009A at 0.7–4 keV. The image has been smoothed with a Gaussian kernel of $\sigma = 1''$, and the point sources are excluded. The yellow cross marks the position of the GRB afterglow. The red labels indicate the positions of the rings 16, 17, 18, and 19 produced by clouds at approximately 8, 10, 14, and 19 kpc, respectively.

No significant background flares were detected, so the full exposure could be analysed. As an alternative to blank-sky background files, we also selected events from the same observation but in a hard energy band (4–10 keV), where no signal from X-ray dust-scattering is expected. To maximize the signal-to-noise ratio of the scattered X-ray rings, the analysis was restricted to the 0.7–4 keV energy band, as done for the *XMM-Newton* data.

2.2. GRB 160623A

GRB 160623A was detected by the *Fermi*/GBM instrument on June 23, 2016, at 05:00:34.23 UT. This burst was also observed above 1 GeV by Fermi/LAT (Vianello & Longo 2016) and detected by Konus-Wind (Frederiks et al. 2016). Approximately 40 ks after the burst, *Swift*/XRT performed its first observation of the GRB afterglow, revealing a dust-scattering ring with a radius of about 3.5′ (Tiengo et al. 2016), attributed to a dust cloud located at approximately 800 pc (see Eq. (4)). In a subsequent *XMM-Newton* observation, six X-ray dust-scattering rings were identified (Pintore et al. 2017). The *XMM-Newton* satellite started observing GRB 160623A approximately two days later on June 24, 2016, at 20:23:46 UT, employing all EPIC cameras in full-frame mode for a duration of 16 hours (Table 1). No more *XMM-Newton* or *Chandra* observations of this field are available.

2.3. GRB 031203

On December 3, 2003, at 22:01:28 UT, GRB 031203 was identified by the Imager aboard the INTEGRAL satellite (IBIS; Gotz et al. 2003). This GRB had a single peak with a duration of 30 s and a peak flux of 1.3×10^{-7} erg s^{-1} cm^{-2} in the 20–200 keV energy range. At the time of the burst, the *Swift* satellite was not yet operational. The *XMM-Newton* observatory reacted

Table 1. Log of the *Chandra* and *XMM-Newton* observations of the GRBs.

	Satellite/instrument	Observation ID	Start time [UTC]	Stop time [UTC]	Exposure [ks]
GRB 221009A	*XMM-Newton*/pn	0913991601 (Obs2)	2022-10-14T05:41:21	2022-10-14T22:52:21	34.0
	Chandra/ACIS	27517	2022-10-17T16:53:32	2022-10-17T23:36:58	21.7
	XMM-Newton/pn	0913991701 (Obs3)	2022-10-30T04:56:37	2022-10-30T21:48:17	34.0
	XMM-Newton/pn	0913991801 (Obs4)	2022-11-01T07:21:37	2022-11-01T21:39:57	35.0
	XMM-Newton/pn	0913991901 (Obs5)	2022-11-10T16:09:14	2022-11-11T21:00:54	87.8
GRB 160623A	*XMM-Newton*/pn	0781100201	2016-06-24T20:23:46	2016-06-25T12:53:464	50.0
	XMM-Newton/MOS				55.0
GRB 031203	*XMM-Newton*/pn	0158160201	2003-12-04T04:09:29	2003-12-04T20:19:40	56.0
	XMM-Newton/MOS				56.0
	XMM-Newton/pn	0163360201	2003-12-06T18:11:07	2003-12-07T09:21:17	37.0
	XMM-Newton/MOS				35.0
	Chandra/ACIS	05298	2004-01-22T21:17:36	2004-01-23T03:44:30	21.5

immediately, while *Chandra* performed its first observations more than a month after the burst.

2.3.1. XMM-Newton observations

A 58 ks observation of the GRB 031203 field with *XMM-Newton* started about six hours after the burst on December 4, 2003, at 04:09:29 UT (Table 1). The *XMM-Newton* satellite captured the GRB on-axis, utilizing all EPIC cameras in full-frame mode.

On December 6, 2003, GRB 031203 was serendipitously observed at an off-axis angle of ∼10′ during a Zeta Puppis pointing (Table 1). Following Eq. (1), the radius of the ring detected by Feng & Fox (2010), which was generated by a cloud at a distance of 9.9 kpc, was expected to be ∼2.4′ after three days, thus remaining fully within the field of view of all three instruments. To maximize the signal-to-noise ratio of the rings, the analysis was confined to the 0.8–2.2 keV energy band, as in Tiengo & Mereghetti (2006).

2.3.2. Chandra observation

The *Chandra* telescope started observing GRB 031203 on January 22, 2004, at 21:17:36 UT with an exposure time of 21.5 ks (Table 1). A 30 ks *Chandra* observation taken on April 18, 2004, was not considered because no detectable X-ray rings were expected more than 100 days after the GRB.

The data were acquired using both ACIS-I and ACIS-S chips in VFAINT mode. No significant background flares were detected during the observation. As in the *XMM-Newton* analysis, we focused on the 0.8–2.2 keV energy. The background blank-sky subtraction was performed separately for CCD S4 and for CCDs I2, I3, S2, and S3 due to the different exposure time of the CCD S4 blank-sky data. To provide additional background estimates, the original event file was filtered both in the 2.2–5 keV and 4–10 keV high energy bands, where negligible dust-scattered X-ray emission is expected.

3. Data analysis and results

We analyzed the X-ray dust-scattering rings of GRB 221009A, GRB 160623A, and GRB 031203, with a particular focus on determining the distances to dust clouds located beyond 5 kpc. For these GRBs, we applied the pseudo-distance distribution method (Tiengo & Mereghetti 2006) to accurately measure the distances of previously discovered dust structures and to search for additional X-ray rings produced by dust in the Perseus, Outer, and OSC arms.

Table 2. Best-fit parameters of the pseudo-distance distribution in the 0.7–4 keV energy band for the GRB 221009A *Chandra* observation.

	Ring 16	Ring 17	Ring 18	Ring 19
Blank-Sky (4 Lorentzians)				
D [kpc]	7.58 ± 0.07	9.76 ± 0.05	14.0 ± 0.1	19.0 ± 0.2
Width [kpc]	0.5 ± 0.1	0.36 ± 0.07	0.9 ± 0.1	1.1 ± 0.3
Counts	124	119	145	86
χ^2/d.o.f.		36.62/22		
p-value		0.026		
4–10 keV background (4 Lorentzians)				
D [kpc]	7.66 ± 0.08	9.75 ± 0.05	13.9 ± 0.1	19.0 ± 0.2
Width [kpc]	0.4 ± 0.1	0.33 ± 0.07	0.8 ± 0.1	1.1 ± 0.3
Counts	93	106	129	76
χ^2/d.o.f.		28.65/22		
p-value		0.155		
Blank-Sky (5 Lorentzians)				
D [kpc]	7.53 ± 0.06	9.1 ± 0.4	14.1 ± 0.1	19.0 ± 0.2
		9.80 ± 0.04		
Width [kpc]	0.3 ± 0.1	1.0 ± 0.4	0.8 ± 0.1	1.1 ± 0.3
		0.16 ± 0.07		
Counts	77	129	139	85
		56		
χ^2/d.o.f.		23.89/19		
p-value		0.200		

Notes. Two background-subtraction methods (blank-sky or 4–10 keV background) and two models (4 or 5 Lorentzians) were adopted.

To produce a pseudo-distance distribution for each detected event, we computed the quantities

$$t_i = T_i - T_0 \tag{2}$$

and

$$\theta_i^2 = (x_i - X_{\rm GRB})^2 + (y_i - Y_{\rm GRB})^2, \tag{3}$$

where x_i, y_i, and T_i are the detector coordinates and the time of arrival of the i-th event, and T_0, $X_{\rm GRB}$, and $Y_{\rm GRB}$ are the GRB time and the detector coordinates, respectively. Using these new coordinates, we computed the pseudo-distance as defined as

$$D_i = 2ct_i/\theta_i^2 = 827\, t_i\,[\rm s]\, \theta_{\rm i}^{-2}\,[\rm arcsec]\,\rm pc \tag{4}$$

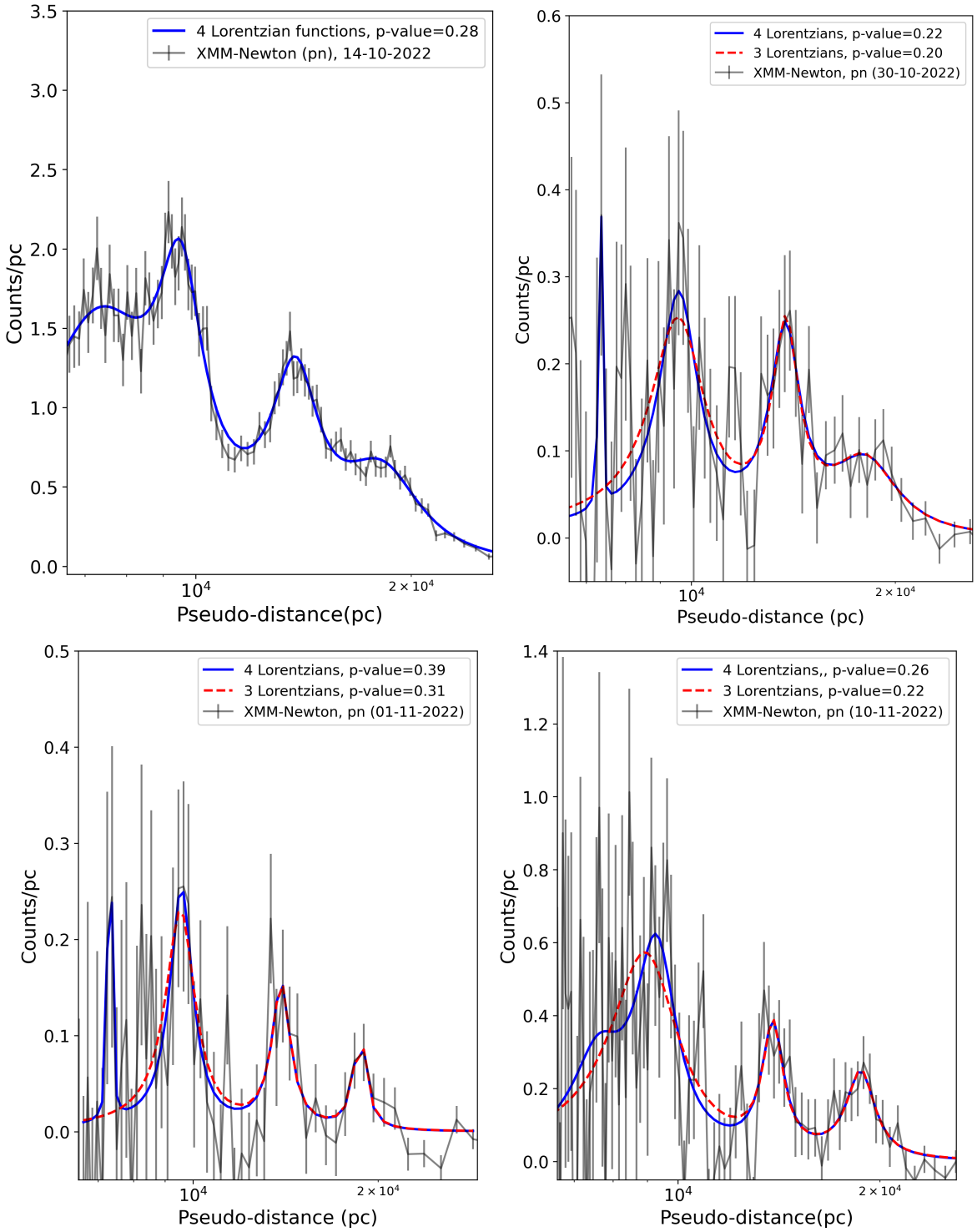


Fig. 2. Pseudo-distance distributions in the 0.7–4 keV energy band for the GRB 221009A observations performed by *XMM-Newton* on October 14 (Obs2, top-left panel), October 30 (Obs3, top-right panel), November 1 (Obs4, bottom-left panel), and November 10 (Obs5, bottom-right panel). The dashed red and solid blue lines indicate the best-fit models with three and four Lorentzian functions, respectively.

For background events, this quantity does not represent a true distance. However, photons from an expanding ring have D_i values that cluster around the distance of the dust-scattering cloud, resulting in a ring appearing as a peak centered at the distance of the dust layer in the pseudo-distance distribution. The data analysis for GRB 221009A, GRB 160623A, and GRB 031203 is detailed in the following subsections.

3.1. GRB 221009A

For GRB 221009A, we created histograms of the pseudo-distances for all the observations and their respective backgrounds, but we limited our analysis only to pseudo-distances larger than 6 kpc. To indicate the peaks and the corresponding rings in the X-ray images, we adopted the nomenclature

introduced in Tiengo et al. (2023), where rings 16, 17, 18, and 19 were identified in this distance range.

For *XMM-Newton* observations, we conducted separate analyses for the data collected by the MOS and pn cameras. After verifying that the results were consistent and that the pn camera provided smaller uncertainties, we chose to present only the pn data. For Obs2, the background-subtracted pseudo-distance was fit in the range from 6 to 30 kpc using a model comprising the sum of four Lorentzian functions, resulting in a good fit (p-value[3] = 0.28; see the top-left panel of Fig. 2). Each Lorentzian component corresponds to a distinct dust cloud, identified in Tiengo et al. (2023) for this GRB within the fit distance range. The distances of these peaks correspond to those of the rings from 16 to 19 reported in Tiengo et al. (2023). Similarly, for Obs3 and Obs4, the pn background-subtracted pseudo-distances were adequately fit (p-value = 0.20 for Obs3 and p-value = 0.31 for Obs4) by the sum of three Lorentzian functions, corresponding to rings 17, 18, and 19 (see Fig. 2).

To check if ring 16 could be detected in these observations as well, we attempted a fit over the same distance range using the sum of four Lorentzian functions. Although the model provided good fits in both cases (Fig. 2), adding an extra Lorentzian did not improve the results, and the best-fit parameters of the three peaks remained consistent with those obtained from the former.

For Obs5, the data were well fit with three Lorentzians (rings 17-19, p-value = 0.22). A four-Lorentzian model was also tested to include ring 16, but the extra peak's distance and width were unconstrained and thus fixed to Obs2 values. This addition did not improve the fit (p-value = 0.26) and left the other parameters unchanged (Fig. 2, bottom right).

For the *Chandra* observation, we derived the histogram of the pseudo-distances and tested both methods for background subtraction. The blank-sky background was simply rescaled by the ratio of the source and background exposure times, while the same observation at high energies was normalized by the ratio of the counts extracted in the 0.7–4 keV and 4–10 keV energy bands from a region free of scattering-ring contamination, corresponding to the 1.3–1.7 kpc distance interval. The background-subtracted data were fit with a model consisting of the sum of four Lorentzian functions over the 6.2–25 kpc distance range. The best-fit results are reported in Table 2. Since the fit obtained with the blank-sky background subtraction was only marginally acceptable, we also added a fifth Lorentzian function to the model. As can be seen in Fig. 3 and Table 2, the additional Lorentzian accounts for a small excess between the first two peaks, with no significant effects on the positions of the four main peaks.

The distances and widths of the dust structures producing rings 17, 18, and 19 derived from the *XMM-Newton* and *Chandra* observations are shown in Fig. 4. A fit with a constant to the distances obtained from the different observations reproduces the data well, indicating that all the measurements – despite being taken with different instruments and at different epochs – are consistent. Similarly, the widths derived from the three late-time *XMM-Newton* observations are in agreement with each other and with the value found by *Chandra*. The width measured in Obs2 is significantly larger, but this can be explained by the fact that in this earlier observation, the rings have smaller radii and the peak width is strongly affected by the instrumental point spread function. The consistency among the other four observations demonstrates that the measured width corresponds to the intrinsic size of the dust cloud and is not dominated by the instrumental spatial resolution.

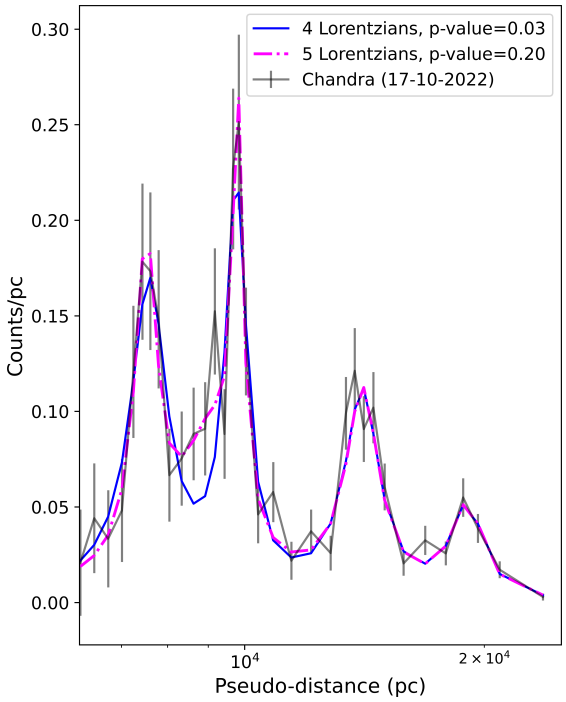


Fig. 3. Pseudo-distance distribution in the 0.7–4 keV energy band for the GRB 221009A *Chandra* observation. The background was subtracted from blank-sky observations. The blue line indicates the best-fit model with four Lorentzian functions, while the magenta line represents the best-fit model with five Lorentzian functions.

3.2. GRB 160623A

The X-ray dust scattering rings around GRB 160623A were previously studied by Pintore et al. (2017), who identified six dust scattering rings, including one at a distance greater than 5 kpc, specifically at 5079 ± 64 pc. In Pintore et al. (2017), the pseudo-distance method was also used to analyze the rings; however, in that case, the background was phenomenologically fit with the sum of two power-law functions, whereas in our analysis, we subtracted the background before fitting. For this GRB, after having verified the consistency of the data from all three cameras[4], we combined all data to minimize uncertainties. We then derived the pseudo-distance distribution from all cameras for both the observation and the background (obtained as described in Sect. 2). The two distributions were subtracted, with normalization applied in a region free from X-ray dust scattering contamination, following the same approach as for GRB 221009A (in this case, the distance interval was 2–3 kpc). From the background-subtracted pseudo-distance distribution at distances greater than 5 kpc, we confirmed the presence of the peak previously identified by Pintore et al. (2017) at $D_1 = 5125 \pm 29$ pc ($\sigma_1 = 410 \pm 47$ pc). Additionally, we detected two more peaks at distances $D_2 = 6909 \pm 56$ pc and $D_3 = 9908 \pm 624$ pc, with widths of $\sigma_2 = 299 \pm 91$ pc and $\sigma_3 = 1027 \pm 190$ pc, respectively. When

[3] The p-value is computed from the χ^2 distribution under the null hypothesis that the model correctly describes the data. Throughout this work, we adopt a p-value threshold of 0.01, below which models are rejected as statistically inconsistent with the null hypothesis.

[4] We also included data from the MOS1 camera despite the damage sustained by two of its external CCDs early in the mission, as we are only interested in features at distances greater than 5 kpc, corresponding to angles smaller than ≃3′, which are fully covered by the central chip.

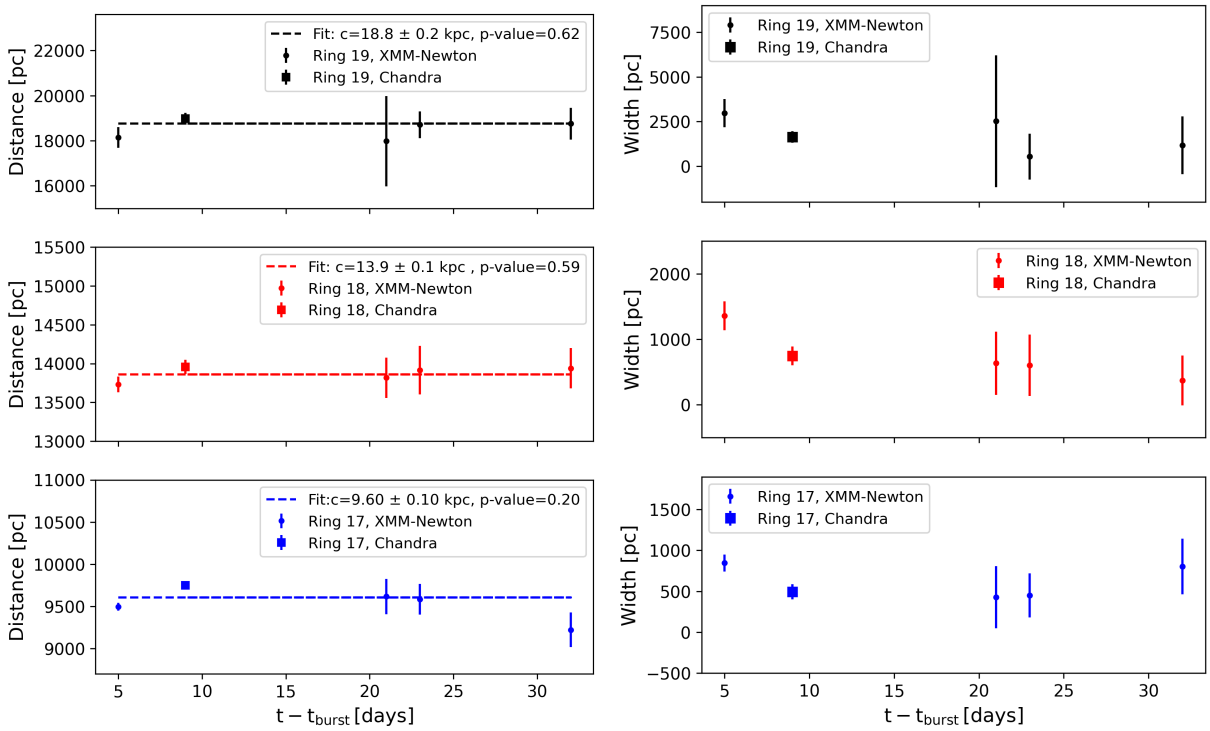


Fig. 4. Distances (left panels) and widths (right panels) of ring 19 (upper panels), ring 18 (central panels), and ring 17 (bottom panels) determined from the *XMM-Newton* (circles) and *Chandra* (squares) observations of GRB 221009A. The dashed line represents the best-fit with a constant.

modeling the data with the sum of only two Lorentzian functions centered at D_1 and D_2, we obtained a p-value of 0.001, whereas a model incorporating three Lorentzian functions yields a p-value of 0.19 (see Fig. 5).

3.3. GRB 031203

The X-ray dust scattering rings around GRB 031203 have been extensively studied over the years. Vaughan et al. (2004) identified two dust scattering rings at distances of less than 2 kpc, a finding later confirmed by Tiengo & Mereghetti (2006) using the pseudo-distance method. A subsequent analysis of the same data by Feng & Fox (2010) reported the discovery of a third ring at a distance of 9.94 ± 0.39 kpc.

We reanalyzed the first *XMM-Newton* observation and, for the first time, applied the pseudo-distance distribution method to both the *Chandra* data and the second *XMM-Newton* observation of this GRB. For *XMM-Newton*, after confirming consistency across all three cameras – following a procedure similar to that used for GRB 160623A – we combined the data of each observation to reduce statistical uncertainties. We then derived the pseudo-distance distributions for both observations and subtracted their corresponding backgrounds (as described in Sect. 2). The background distributions were normalized in a region free from X-ray dust scattering contamination, specifically between 4 and 7 kpc, in line with the method used for GRB 221009A and GRB 160623A. By fitting the background-subtracted pseudo-distance distribution of the first observation in the 4–25 kpc range, we confirmed the presence of the peak identified, albeit with a different method, by Feng & Fox (2010). Our analysis yielded a dust cloud distance of 9.9 ± 0.4 kpc and a width of $\sigma = 1.5 \pm 0.6$ kpc, with a fit p-value of 0.30 (see the upper panel Fig. 6). The same peak is also visible in the second *XMM-Newton* observation, though with a lower significance. Fitting its background-subtracted pseudo-distance distribution, we found a peak at 8.7 ± 0.8 kpc with a width of $\sigma = 1.2 \pm 0.7$ kpc. This fit returned a p-value of 0.05, while a fit using a constant model resulted in a much lower p-value of 0.0005 (see the bottom panel of Fig. 6). The weighted average of these two measurements provides a distance of 9.7 ± 0.4 kpc.

For the *Chandra* observation, we derived histograms of the pseudo-distances by subtracting both the blank-sky and high-energy backgrounds, but no significant dust-scattered emission was detected. In the latter case, the background pseudo-distance values were normalized by the ratio of the total counts in the 0.8–2.2 keV band to those in the 2.2–5 keV range, extracted from a region free of scattering ring contamination (corresponding to distances in the 12–15 kpc interval). The fit of the background-subtracted distribution with a constant was perfectly consistent with no signal in the 3.5–20 kpc distance range ($y = -0.007 \pm 0.004$, χ^2/d.o.f. = 27.43/35, p-value = 0.82).

4. Discussion

By analyzing the expanding X-ray scattering rings of GRB 221009A, GRB 160623A, and GRB 031203, we were able to map the outer structure of the Milky Way with an unprecedented level of precision. Unlike the most commonly used methods that rely on kinematic models, the dust scattering rings provide a direct geometric measurement of the distance to dust clouds along the line of sight. Owing to the good angular resolution of our X-ray data, we could measure not only the distance but also the spatial thickness of the spiral arms, as the shape of the peaks in the pseudo-distance distributions reflects the radial distribution of dust within each arm.

In Fig. 7, we overlay the three directions sampled by the selected GRBs on the Milky Way picture reported in Sun et al. (2024), which is based on the Reid et al. (2019) rotation curve.

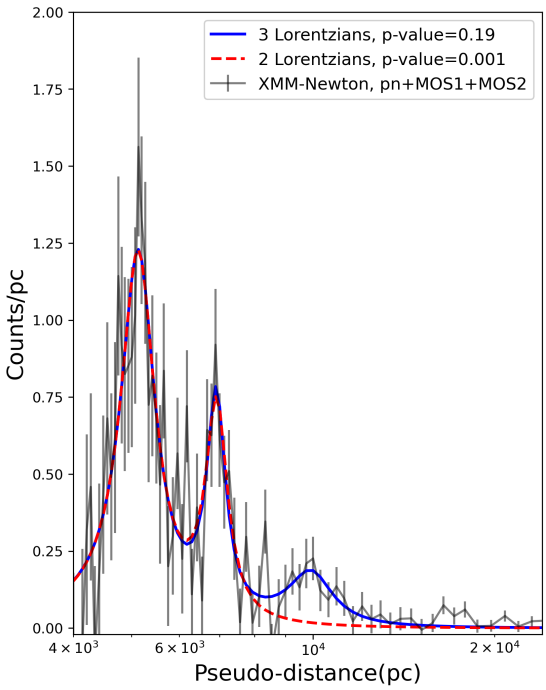


Fig. 5. Pseudo-distance distributions in the 0.7–4 keV energy band for the GRB 160623A *XMM-Newton* observations of June 24 between 4 and 20 kpc. The solid blue line indicates the best-fit model with three Lorentzian functions. The dashed red line indicates the best-fit model with two Lorentzian functions.

As indicated by the cyan dots in the figure, our analysis allowed us to probe the structure of the Perseus, Outer, and OSC arms. In the following, we compare our results with the distances of Galactic structures derived from H I/CO data in the same directions, assuming different Galactic rotation curves, and we discuss their implications on the characterization of each spiral arm.

4.1. Comparison with H I/CO data and kinematic models

Both H I and CO emission can trace the large-scale structure of spiral arms across the Galaxy, but their interpretation relies on Galactic kinematic models, which introduce systematic uncertainties at large distances. Figure 8 presents a direct comparison of our distance measurements (blue solid lines) for the directions of GRB 221009A and GRB 160623A with H I data from the EBHIS survey (Winkel et al. 2016), which covers the entire northern sky. For the GRB 031203 direction, located in the southern hemisphere, a similar comparison was made using H I data from the GASS survey (HI4PI Collaboration 2016). The H I data were extracted from a 15′ circular region around the GRB directions for GRB 221009A and GRB 160623A, and a 30′ region for GRB 031203.

The local standard of rest velocities of the H I clouds were deprojected into distances using two different Galactic rotation curve models: Reid et al. (2019), which is the one used in Fig. 7, and Clemens (1985). These two rotation curves are among the most widely used in the literature. The model of Clemens (1985) is based on CO observations and adopts $R_0 = 8.5$ kpc and $\Theta_0 = 220\,\mathrm{km\,s^{-1}}$, while that of Reid et al. (2019) is derived from maser parallaxes of high-mass star-forming regions and assumes $R_0 = 8.15$ kpc and $\Theta_0 = 236\,\mathrm{km\,s^{-1}}$. For each velocity, the deprojection yields two possible distances that are displayed along the two horizontal axes in Fig. 8.

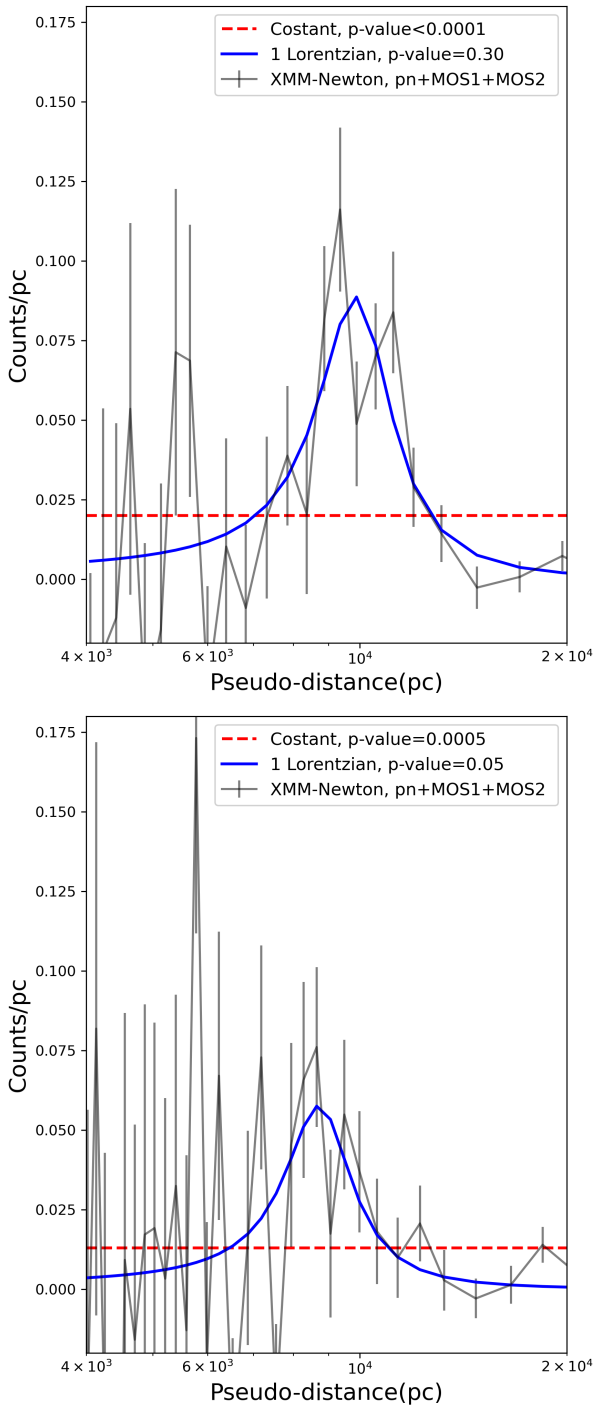


Fig. 6. Pseudo-distance distributions in the 0.8–2.2 keV band for the *XMM-Newton* observations of GRB 031203. The solid blue line shows the best-fit with a Lorentzian function, and the dashed red line shows the best-fit with a constant. Upper panel: Observation performed on December 4. Bottom panel: Observation performed on December 6.

In general, the Galactic rotation curve model of Reid et al. (2019) provides a better match to the locations of the dust clouds derived in this work compared to the Clemens (1985) model. However, at the expected distances of the Outer and the OSC arms, even the Reid et al. (2019) model appears to diverge systematically from the distribution of the dust clouds, suggesting possible deviations in the assumed Galactic dynamics. In particular, in the directions of GRB 221009A and GRB 160623A, the peaks obtained from the Reid et al. (2019) model are systematically at

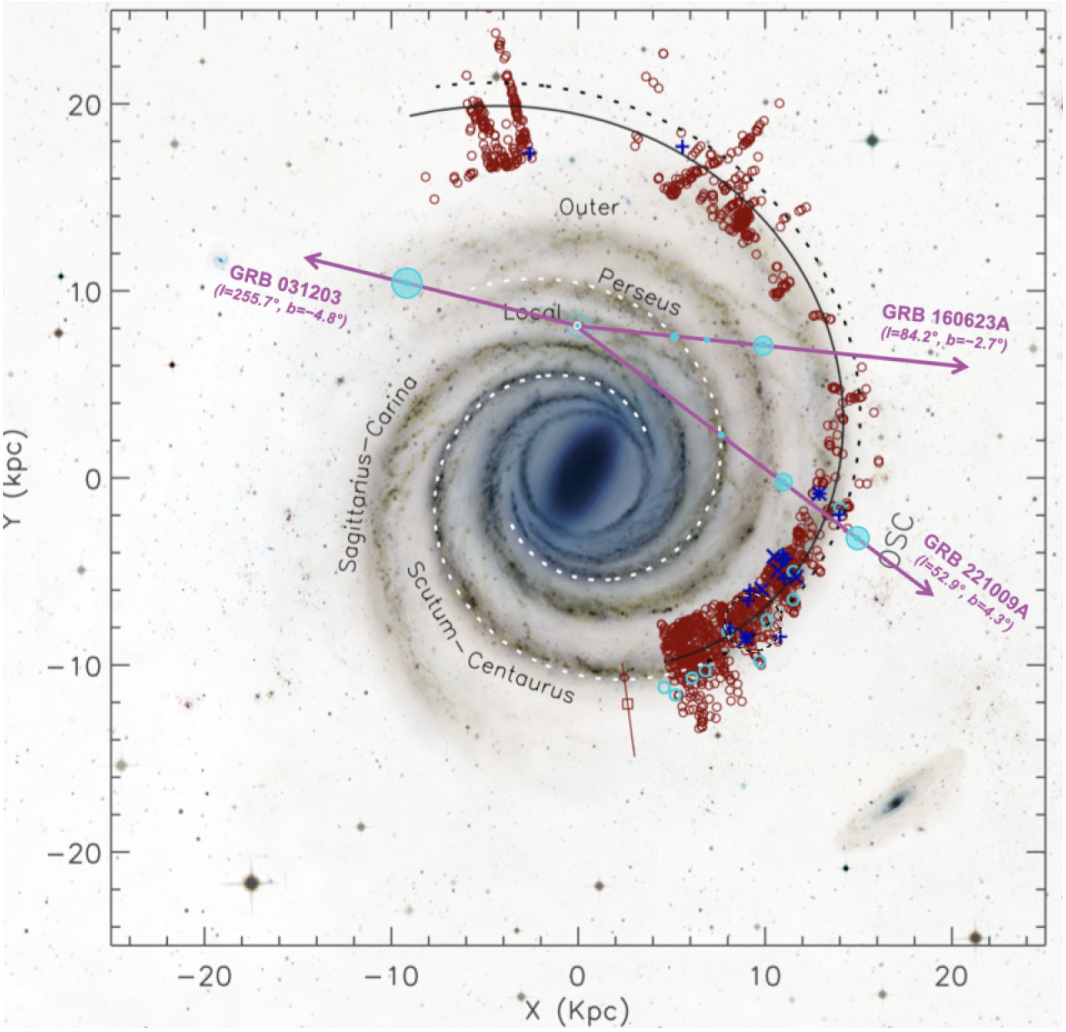


Fig. 7. Spiral structure of the Milky Way, adapted from Sun et al. (2024). The background map shows the distribution of molecular clouds and high-mass star-forming regions. Red and cyan circles indicate the 1306 MCs from Sun et al. (2024) and ten molecular clouds from Dame & Thaddeus (2011), respectively. The dashed white lines represent the symmetrical Scutum-Centaurus and Perseus arms. The red square with the error bar marks the only directly measured trigonometric parallax for the OSC Arm (Sanna et al. 2017), while the diamond represents the kinematically derived location of the same high-mass star-forming region. Blue pluses and crosses indicate distant H II regions and star-forming masers, respectively. Our measured distances are overlaid as cyan dots, showing the positions and the widths (surrounding red circles) of the spiral arms as determined from X-ray scattering rings of GRB 221009A (rings 17, 18, and 19), GRB 160623A, and GRB 031203. The directions of these three GRBs are highlighted in purple.

smaller distances than those derived from X-ray data, whereas the Clemens (1985) rotation curve always provides larger distances.

We also examined the sight lines toward the three GRBs using the CO survey by Dame et al. (2001), extracting data in the GRB directions and averaging over a 1° region. However, no significant CO emission was detected at distances greater than 5 kpc.

4.2. Perseus Arm

In Fig. 7, we show the directions of the three GRBs cross the Perseus Arm. GRB 031203 is located very close to the end of this spiral arm, and no X-ray ring at the corresponding distance was detected. This result is consistent with the lack of a prominent peak at the same distance in the GASS data (bottom panel of Fig. 8), which confirms that a negligible amount of dust content is present in the Perseus Arm in the GRB direction ($l = 256°$, $b = -5°$).

Dust scattering rings can instead be associated with the Perseus Arm in the X-ray observations of GRB 221009A and GRB 160623A, allowing us to accurately measure its distance toward their directions: 9.6 ± 0.1 and 5.12 ± 0.03 kpc, respectively. Both of these independent measurements are fully consistent with a symmetric inner-Galaxy spiral structure (Vallée 2008), as shown by the dashed white lines in Fig. 7.

The EBHIS data in the direction of GRB 221009A (top panel of Fig. 8) display a clear peak at ∼10 kpc, with a slightly better agreement with X-ray data if the Clemens (1985) rotation curve is adopted. The EBHIS data toward GRB 160623A (middle panel of Fig. 8) indicate a complex structure in the Perseus Arm. In particular, we observed a broad bump at a distance consistent with that derived from the dust-scattering ring reported by Pintore et al. (2017) as well as a smaller peak compatible with the new X-ray signal detected at 6.9 kpc. The detection of significant amounts of dust at the Galactic longitudes of GRB 221009A ($l = 53°$) and GRB 160623A ($l = 84°$) is particularly interesting because they are close to the edges of the Perseus Arm gap, which is a ∼6 kpc section of the spiral arm with a reduced massive star formation activity (Zhang et al. 2013; Sakai et al. 2022).

4.3. Outer Arm

The Outer Arm is the only spiral arm that could be mapped in all three directions. The detection of a significant excess in the pseudo-distance distributions derived from two different *XMM-Newton* observations of GRB 031203 with distance and width consistent with those expected for the Outer Arm in this direction allowed us to confirm that this spiral arm extends up to $l = 256°$ and $b = -5°$. A clear signal with a double-peaked profile was detected in the GASS data (bottom panel of Fig. 8). Adopting the Reid et al. (2019) rotation curve, the inferred distance is comparable to that derived from the X-ray analysis, whereas assuming the kinematic parameters of Clemens (1985) yields a significantly larger value.

The distances measured for ring 18 in GRB 221009A (13.9 ± 0.1 kpc) and for the smallest newly discovered ring in GRB 160623A (9.9 ± 0.6 kpc) exceed those predicted by the model in Fig. 7. This suggests that the Reid et al. (2019) rotation curve used by Sun et al. (2024) to derive the Milky Way structure underestimates the distance of the Outer Arm in this direction. In contrast, the top and middle panels of Fig. 8 indicate that the opposite is valid for the Clemens (1985) rotation curve.

4.4. Outer Scutum-Centaurus arm

The OSC Arm was clearly detected only in the direction of GRB 221009A, positioning the arm farther than both models shown in Fig. 7. The dashed black line in the figure represents the extrapolation of the symmetrical spiral structure by Vallée (2008), and the solid black line is derived from the analysis of a selection of molecular clouds (Sun et al. 2024). This discrepancy is confirmed by the EBHIS data with distances derived using the same rotation curve (Reid et al. 2019), while an excessive distance was obtained assuming the Clemens (1985) kinematic parameters (top panel of Fig. 8). Since the same effect was observed also for the Outer Arm, our analysis suggests a revision of both rotation curves to better reproduce the structure of the two outer arms of our Galaxy in the first quadrant.

The other distance measurements of individual objects reported in Fig. 7 are spread over a relatively wide distance range and are affected by large uncertainties. The choice of a specific rotation curve (Reid et al. 2019 in this case) leads to an underestimation of all distances derived from kinematic methods. On the other hand, the most robust distance measurement previously reported for this arm ($20.4^{+2.8}_{-2.2}$ kpc; Sanna et al. 2017), based on the parallax of a water maser source at small Galactic longitude (red square with error bar in Fig. 7), has an order of magnitude larger uncertainty than our measurement (19.0 ± 0.2 kpc from *Chandra* data). Moreover, the peak width of ∼2 kpc reflects the radial extent of dust along the line of sight, supporting the interpretation that it traces the arm's thickness rather than a single localized cloud.

The detection of a peak at 19 kpc in the pseudo-distance distribution might be surprising even for an exceptionally bright event as GRB 221009A since its latitude of 4.3° implies the presence of a significant amount of dust 1.4 kpc above the Galactic plane. However, this portion of the OSC Arm is significantly inclined, with an average latitude of ∼3° and a width >2° at the longitude of GRB 221009A (Dame & Thaddeus 2011). Therefore, the non-detection of a similar structure in the GRB 160623A is justified not only by the lower fluence of this GRB but also by its negative latitude ($b = -2.7°$).

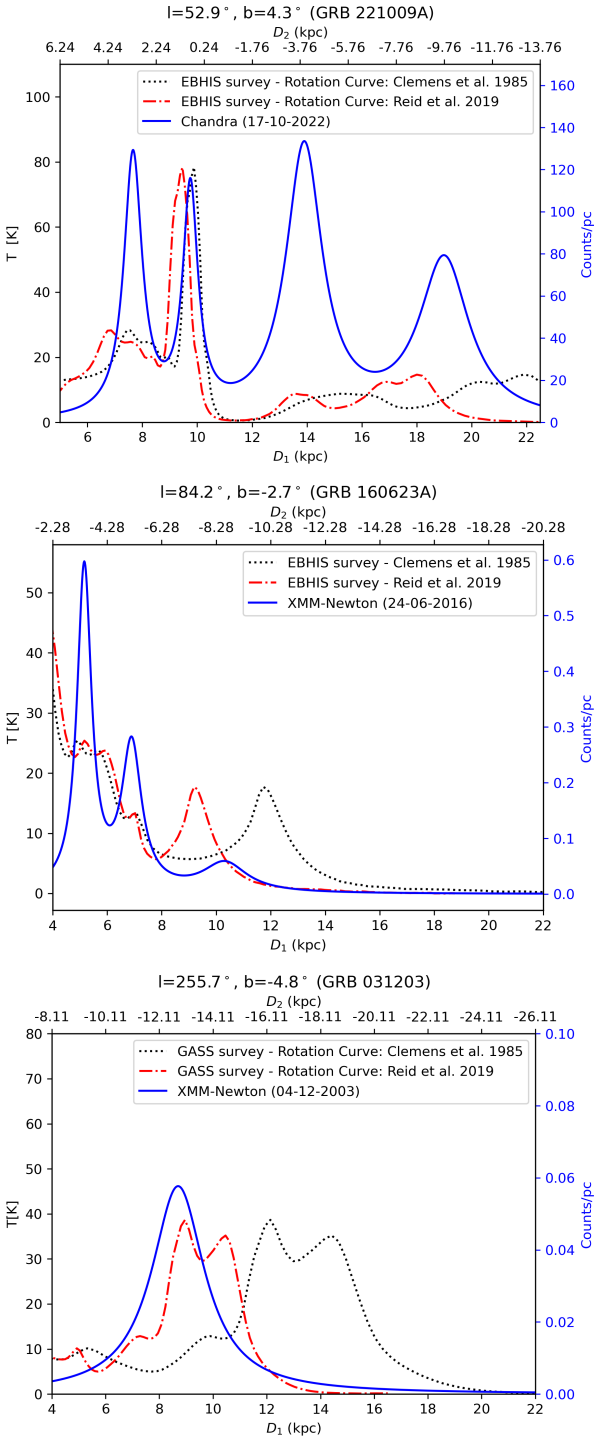


Fig. 8. Comparison of our dust distance measurements (solid blue lines) in the directions of GRB 221009A (upper panel), GRB 160623A (central panel), and GRB 031203 (lower panel) with H I data from the EBHIS survey (Winkel et al. 2016) for GRB221009A and GRB100623A and from the GASS survey (HI4PI Collaboration 2016) for GRB031203. The local standard of rest velocities have been deprojected into distances using two different models for the Galactic rotation curve: Reid et al. (2019, dot-dashed red lines) and Clemens (1985, dotted black lines).

5. Conclusions

By combining *XMM-Newton* and *Chandra* observations of three low-latitude GRBs in different directions, we have mapped

multiple Galactic spiral arms, cross-checked distances, and provided robust constraints on the large-scale geometry of the outer Galaxy. In particular, our measurement of the OSC Arm places it at 19.0 ± 0.2 kpc, achieving a precision far superior to the previous maser-parallax measurements ($20.4^{+2.8}_{-2.2}$ kpc; Sanna et al. 2017).

Although low-latitude GRBs as bright as GRB 221009A are very unlikely to repeat soon, future X-ray observatories such as *AXIS* (Reynolds et al. 2023) and *New Athena* (Cruise et al. 2025) will enable systematic campaigns of GRB follow-ups, which, thanks to their higher sensitivity, will expand the sample of X-ray rings generated by dust in the outskirts of the Milky Way. This will allow precise mapping of interstellar clouds traced by dust along more sight lines, complementing the 3D dust distributions derived from extinction studies in the optical and infrared band based, for example, on future Gaia Data Releases and the Galactic Plane Survey that will be performed by the *Nancy Grace Roman Space Telescope* (Akeson et al. 2019).

Acknowledgements. This publication was produced while B.V. attending the PhD program in Space Science and Technology at the University of Trento, Cycle XXXVIII, with the support of a scholarship financed by the Ministerial Decree no. 351 of 9th April 2022, based on the NRRP – funded by the European Union – NextGenerationEU – Mission 4 "Education and Research", Component 1 "Enhancement of the offer of educational services: from nurseries to universities" – Investment 4.1 "Extension of the number of research doctorates and innovative doctorates for public administration and cultural heritage". This paper and related research have been conducted during and with the support of the Italian national inter-university PhD programme in Space Science and Technology – University of Trento/IUSS Pavia. AB acknowledges the financial support of INAF through the initiative "IAF Astronomy Fellowships in Italy" (grant name MEGASKAT).

References

Akeson, R., Armus, L., Bachelet, E., et al. 2019, arXiv e-prints [arXiv:1902.05569]
Anderson, L. D., Bania, T. M., Balser, D. S., & Rood, R. T. 2011, ApJS, 194, 32
Barnes, D. G., Staveley-Smith, L., de Blok, W. J. G., et al. 2001, MNRAS, 322, 486
Breen, S. L., Fuller, G. A., Caswell, J. L., et al. 2015, MNRAS, 450, 4109
Chen, B.-Q., Huang, Y., Yuan, H.-B., et al. 2018, MNRAS, 483, 4277
Clemens, D. P. 1985, ApJ, 295, 422
Cruise, M., Guainazzi, M., Aird, J., et al. 2025, Nat. Astron., 9, 36
Dame, T. M., & Thaddeus, P. 2011, ApJ, 734, L24
Dame, T. M., & Thaddeus, P. 2022, ApJS, 262, 5
Dame, T. M., Hartmann, D., & Thaddeus, P. 2001, ApJ, 547, 792
Dichiara, S., Gropp, J. D., Kennea, J. A., et al. 2022, GRB Coordinates Network, 32632, 1
Eilers, A.-C., Hogg, D. W., Rix, H.-W., & Ness, M. K. 2019, ApJ, 871, 120
Feng, L., & Fox, D. B. 2010, MNRAS, 404, 1018
Frederiks, D., Golenetskii, S., Aptekar, R., et al. 2016, GRB Coordinates Network, 19554, 1
Fruscione, A., McDowell, J. C., Allen, G. E., et al. 2006, in SPIE Conference Series, eds. D. R. Silva, & R. E. Doxsey, SPIE Conf. Ser., 6270, 62701V
Gabriel, C., Denby, M., Fyfe, D. J., et al. 2004, in Astronomical Data Analysis Software and Systems (ADASS) XIII, eds. F. Ochsenbein, M. G. Allen, & D. Egret, ASP Conf. Ser., 314, 759
Gaia Collaboration (Prusti, T., et al.) 2016, A&A, 595, A1
Gastaldello, F., Marelli, M., Molendi, S., et al. 2022, ApJ, 928, 168
Gotz, D., Mereghetti, S., Beck, M., Borkowski, J., & Mowlavi, N. 2003, GRB Coordinates Network, 2459, 1
Green, J. A., Caswell, J. L., Fuller, G. A., et al. 2009, MNRAS, 392, 783
Green, G. M., Schlafly, E., Zucker, C., Speagle, J. S., & Finkbeiner, D. 2019, ApJ, 887, 93
Heyer, M. H., Carpenter, J. M., & Snell, R. L. 2001, ApJ, 551, 852
HI4PI Collaboration (Ben Bekhti, N., et al.) 2016, A&A, 594, A116
Hottier, C., Babusiaux, C., & Arenou, F. 2020, A&A, 641, A79
Hou, L. G., & Han, J. L. 2014, A&A, 569, A125
Jansen, F., Lumb, D., Altieri, B., et al. 2001, A&A, 365, L1
Kalberla, P. M. W., & Haud, U. 2015, A&A, 578, A78
Kalberla, P. M. W., Burton, W. B., Hartmann, D., et al. 2005, A&A, 440, 775
Kalberla, P. M. W., McClure-Griffiths, N. M., Pisano, D. J., et al. 2010, A&A, 521, A17
Lallement, R., Vergely, J. L., Babusiaux, C., & Cox, N. L. J. 2022, A&A, 661, A147
Lesage, S., Veres, P., Briggs, M. S., et al. 2023, ApJ, 952, L42
Levine, E. S., Blitz, L., & Heiles, C. 2006, Science, 312, 1773
Lombardi, M., Alves, J., & Lada, C. J. 2006, A&A, 454, 781
McClure-Griffiths, N. M., Pisano, D. J., Calabretta, M. R., et al. 2009, ApJS, 181, 398
Miville-Deschênes, M.-A., Murray, N., & Lee, E. J. 2017, ApJ, 834, 57
Negro, M., Di Lalla, N., Omodei, N., et al. 2023, ApJ, 946, L21
Oort, J. H., Kerr, F. J., & Westerhout, G. 1958, MNRAS, 118, 379
Peek, J. E. G., Heiles, C., Douglas, K. A., et al. 2011, ApJS, 194, 20
Persic, M., Salucci, P., & Stel, F. 1996, MNRAS, 281, 27
Pintore, F., Tiengo, A., Mereghetti, S., et al. 2017, MNRAS, 472, 1465
Reid, M. J., Menten, K. M., Brunthaler, A., et al. 2019, ApJ, 885, 131
Reynolds, C. S., Kara, E. A., Mushotzky, R. F., et al. 2023, in UV, X-Ray, and Gamma-Ray Space Instrumentation for Astronomy XXIII, eds. O. H. Siegmund, & K. Hoadley, SPIE Conf. Ser., 12678, 126781E
Rezaei Kh., S., Bailer-Jones, C. A. L., Soler, J. D., & Zari, E. 2020, A&A, 643, A151
Rezaei, S. K., Beuther, H., Benjamin, R. A., et al. 2024, A&A, 692, A255
Roman-Duval, J., Jackson, J. M., Heyer, M., Rathborne, J., & Simon, R. 2010, ApJ, 723, 492
Sakai, N., Nakanishi, H., Kurahara, K., et al. 2022, PASJ, 74, 209
Sale, S. E., & Magorrian, J. 2018, MNRAS, 481, 494
Sanna, A., Reid, M. J., Dame, T. M., Menten, K. M., & Brunthaler, A. 2017, Science, 358, 227
Schlafly, E. F., Finkbeiner, D. P., Schlegel, D. J., et al. 2010, ApJ, 725, 1175
Schlegel, D. J., Finkbeiner, D. P., & Davis, M. 1998, ApJ, 500, 525
Schuller, F., Urquhart, J. S., Csengeri, T., et al. 2021, MNRAS, 500, 3064
Šiljeg, B., Bošnjak, Ž., Jelić, V., et al. 2023, MNRAS, 526, 2605
Strüder, L., Briel, U., Dennerl, K., et al. 2001, A&A, 365, L18
Sun, Y., Yang, J., Zhang, S., et al. 2024, ApJ, 977, L35
Tiengo, A., & Mereghetti, S. 2006, A&A, 449, 203
Tiengo, A., Vianello, G., Esposito, P., & Salvaterra, R. 2016, GRB Coordinates Network, 19559, 1
Tiengo, A., Pintore, F., Vaia, B., et al. 2023, ApJ, 946, L30
Turner, M. J. L., Abbey, A., Arnaud, M., et al. 2001, A&A, 365, L27
Vaia, B., Bošnjak, Ž., Bracco, A., et al. 2025, A&A, 696, A9
Vallée, J. P. 2008, AJ, 135, 1301
Vasilopoulos, G., Karavola, D., Stathopoulos, S. I., & Petropoulou, M. 2023, MNRAS, 521, 1590
Vaughan, S., Willingale, R., O'Brien, P. T., et al. 2004, ApJ, 603, L5
Vianello, G., & Longo, F. 2016, GRB Coordinates Network, 20229, 1
Weisskopf, M. C., Tananbaum, H. D., Van Speybroeck, L. P., & O'Dell, S. L. 2000, in X-Ray Optics, Instruments, and Missions III, eds. J. E. Truemper, & B. Aschenbach, SPIE Conf. Ser., 4012, 2
Williams, M. A., Kennea, J. A., Dichiara, S., et al. 2023, ApJ, 946, L24
Winkel, B., Kerp, J., Flöer, L., et al. 2016, A&A, 585, A41
Zhang, B., Reid, M. J., Menten, K. M., et al. 2013, ApJ, 775, 79
Zucker, C., Saydjari, A. K., Speagle, J. S., et al. 2025, ApJ, 992, 39